AFRL-RZ-WP-TP-2012-0062

PARTICLE IMAGE VELOCIMETRY IN AN ISOTHERMAL AND EXOTHERMIC HIGH-SPEED CAVITY (POSTPRINT)

Steven G. Tuttle

U.S. Naval Research Laboratory

Kuang-Yu Hsu

Innovative Scientific Solutions, Inc.

Campbell D. Carter

Propulsion Sciences Branch
Aerospace Propulsion Division

FEBRUARY 2012

AIR FORCE RESEARCH LABORATORY
PROPULSION DIRECTORATE
WRIGHT-PATTERSON AIR FORCE BASE, OH 45433-7251
AIR FORCE MATERIEL COMMAND
UNITED STATES AIR FORCE

REPORT DOCUMENTATION PAGE

1. REPORT DATE *(DD-MM-YY)*	2. REPORT TYPE	3. DATES COVERED *(From - To)*
February 2012	Conference Paper Postprint	01 October 2010 – 01 February 2012

4. TITLE AND SUBTITLE
PARTICLE IMAGE VELOCIMETRY IN AN ISOTHERMAL AND EXOTHERMIC HIGH-SPEED CAVITY (POSTPRINT)

5a. CONTRACT NUMBER
In-house

5b. GRANT NUMBER

5c. PROGRAM ELEMENT NUMBER
61102F

6. AUTHOR(S)
Steven G. Tuttle (U.S. Naval Research Laboratory)
Kuang-Yu Hsu (Innovative Scientific Solutions, Inc.)
Campbell D. Carter (AFRL/RZAS)

5d. PROJECT NUMBER
2308

5e. TASK NUMBER
AI

5f. WORK UNIT NUMBER
2308AI00

7. PERFORMING ORGANIZATION NAME(S) AND ADDRESS(ES)

U.S. Naval Research Laboratory
Washington, DC 20375

Innovative Scientific Solutions, Inc.
Dayton, OH 45440

Propulsion Sciences Branch (AFRL/RZAS)
Aerospace Propulsion Division
Air Force Research Laboratory
Propulsion Directorate
Wright-Patterson Air Force Base, OH 45433-7251
Air Force Materiel Command, United States Air Force

8. PERFORMING ORGANIZATION REPORT NUMBER
AFRL-RZ-WP-TP-2012-0062

9. SPONSORING/MONITORING AGENCY NAME(S) AND ADDRESS(ES)
Air Force Research Laboratory
Propulsion Directorate
Wright-Patterson Air Force Base, OH 45433-7251
Air Force Materiel Command
United States Air Force

10. SPONSORING/MONITORING AGENCY ACRONYM(S)
AFRL/RZAS

11. SPONSORING/MONITORING AGENCY REPORT NUMBER(S)
AFRL-RZ-WP-TP-2012-0062

12. DISTRIBUTION/AVAILABILITY STATEMENT
Approved for public release; distribution unlimited.

13. SUPPLEMENTARY NOTES
Conference paper submitted to the Proceedings of the 50th AIAA Aerospace Sciences Meeting, held in Nashville, TN on January 9 - 12, 2012.
PA Case Number: 88ABW-2011-6130; Clearance Date: 18 Nov 2011. Report contains color.

14. ABSTRACT

Particle image velocimetry measurements were taken at the center plane of a high-speed cavity combustor in isothermal and reacting conditions at fuel flows corresponding to medium, medium-high, and high power conditions with supersonic bulk flow velocities. Calculation of the instantaneous and time-averaged particle traces, vorticity, principal stresses, and divergence of the velocity field revealed a highly unsteady, three-dimensional flow with coherent eddy structures formed at the stagnation zone of the shear layer against the downstream ramp of the cavity that appear to be convected upstream in the cavity. Comparison of the shear layer location, thickness, and reattachment stagnation point revealed a number of changes in the mean and unsteady velocity behavior that were dependent on the heat release in the cavity and shear layer. As combustion shifted from the cavity at medium power into the shear layer at high power, the volumetric expansion compressed the primary recirculation zone and thickened the downstream boundary layer at the cavity exit. Combustion in the cavity tended to attenuate cavity and shear layer unsteadiness. When the combustion shifted to the shear layer, velocity unsteadiness increased, though not to the amplitudes measured without combustion.

15. SUBJECT TERMS

16. SECURITY CLASSIFICATION OF:

a. REPORT	b. ABSTRACT	c. THIS PAGE
Unclassified	Unclassified	Unclassified

17. LIMITATION OF ABSTRACT:
SAR

18. NUMBER OF PAGES
26

19a. NAME OF RESPONSIBLE PERSON (Monitor)
Campbell D. Carter

19b. TELEPHONE NUMBER *(Include Area Code)*
N/A

50th AIAA Aerospace Sciences Meeting including the New Horizons Forum and Aerospace Exposition
09 - 12 January 2012, Nashville, Tennessee

AIAA 2012-0330

Particle Image Velocimetry in an Isothermal and Exothermic High-Speed Cavity

Steven G. Tuttle[*]
U.S. Naval Research Laboratory, Washington, DC 20375

Campbell D. Carter[†]
U.S. Air Force Research Laboratory, Wright-Patterson Air Force Base, Ohio 45433

Kuang-Yu Hsu[‡]
Innovative Scientific Solutions, Inc., Dayton, Ohio 45440

Particle image velocimetry measurements were taken at the center plane of a high-speed cavity combustor in isothermal and reacting conditions at fuel flows corresponding to medium, medium-high, and high power conditions with supersonic bulk flow velocities. Calculation of the instantaneous and time-averaged particle traces, vorticity, principal stresses, and divergence of the velocity field revealed a highly unsteady, three-dimensional flow with coherent eddy structures formed at the stagnation zone of the shear layer against the downstream ramp of the cavity that appear to be convected upstream in the cavity. Comparison of the shear layer location, thickness, and reattachment stagnation point revealed a number of changes in the mean and unsteady velocity behavior that were dependent on the heat release in the cavity and shear layer. As combustion shifted from the cavity at medium power into the shear layer at high power, the volumetric expansion compressed the primary recirculation zone and thickened the downstream boundary layer at the cavity exit. Combustion in the cavity tended to attenuate cavity and shear layer unsteadiness. When the combustion shifted to the shear layer, velocity unsteadiness increased, though not to the amplitudes measured without combustion.

I. Introduction

CAVITY combustors may be found in a number of applications, from ground-based power generation to aircraft engines. A cavity adjacent to any flow path results in the formation of a recirculation zone with a much longer fluid mechanical residence time than the bulk flow of the duct, making cavities ideal pilot regions to provide heat and radicals for combustion to propagate into the bulk flow. Supersonic combustion systems typically employ some type of cavity combustor to provide heat and radicals to ignite fuel in the free-stream. Because of the small aerodynamic time scales associated with supersonic flows and the interference of oblique shocks upstream and downstream, combustion is generally partially premixed and critically dependent on the location, method, and quantity of fuel injection.

In a typical high-speed combustor flow path design, a primary recirculation zone is produced either by a fuel injector strut inserted across the flow or, more typically, some type of wall step or cavity as the main engine stream flows past. Hot combustion products are trapped in these wake regions, where they circulate upstream to mix with cooler reactants and stabilize the combustion in the main flow. Flame-holders are fueled either directly by injection into the wake region or from upstream by a combination of fuel ports injecting perpendicularly and/or at some lesser angle to the flow, as shown in Figure 1.

[*] Mechanical Engineer, Code 6185, 4555 Overlook Avenue SW. Senior AIAA Member
[†] Principal Aerospace Engineer, AFRL/RZAS, 1950 Fifth Street. Associate Fellow AIAA
[‡] Senior Research Scientist, 2766 Indian Ripple Road. Associate Fellow AIAA

American Institute of Aeronautics and Astronautics
Approved for public release; distribution unlimited
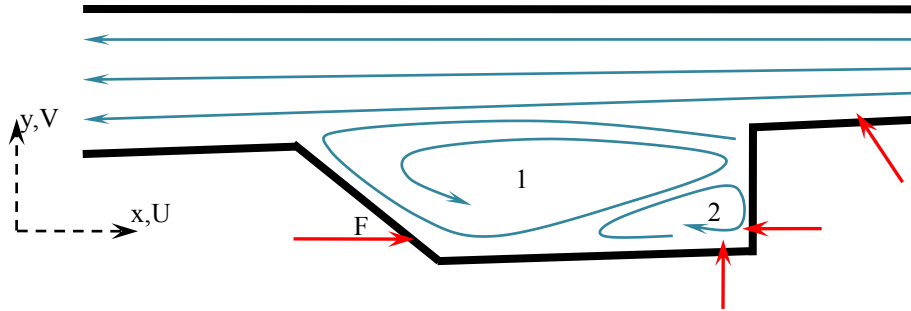
Figure 1: Idealized layout of cavity flow with stream lines, primary (1) recirculation zone, secondary (2) recirculation zone, and possible fuel injection sites (F).

Various aspects of the aerodynamics and chemistry complicate flame stability, including the relatively long reaction time scales associated with hydrocarbon fuels, even with the high temperatures found in supersonic combustors. Furthermore, the short residence times in both the free-stream and cavity ensure that the fuel is not fully mixed when it reaches a flame [1,2]. Anchoring partially premixed flames, which are dependent on mass transport, with minimal pressure loss and such small aerodynamic residence times, is a challenge that may be further encumbered by a changing flowfield as the duct flow accelerates from subsonic to supersonic conditions. In the subsonic regime, the static temperature is sufficiently low that the chemical kinetics, as well as mixing, influence flame stability. At the higher static temperatures (but lower static pressures) found in the supersonic regime, the chemical time scales are much smaller, but the fuel mixing problems are exacerbated by the lower aerodynamic residence times [3].

A number of investigations have focused on the isothermal mixing behavior and combustion species of supersonic cavity combustors [1-4], while studies reporting velocity measurements for reacting flow have been few and specific to particular geometries or conditions [5,6]. Development of high-speed combustor technology at scales relevant to practical engineering applications requires measurements in prototypical combustor geometries that may be applied to practical designs. Therefore, both fuel mixing and velocity measurements in both isothermal and reacting conditions are required to characterize behavior at ignition and stable operating conditions. Studies with other recirculating and wake geometries have highlighted how shear layers and recirculating flows are altered by heat release; both the flow field and the coupled fuel transport are altered by the changed molecular viscosity and the dilatation of the reacting flow, as well as the baroclinicity across the reaction zone [7,8,9]

A. Objective and Scope of Investigation

The purpose of this investigation is to characterize the instantaneous velocity within a high-speed cavity combustor and the adjacent shear layer in both reacting and non-reacting conditions in order to understand mechanisms that stabilize combustion within the cavity and propagate combustion into the free-stream. This study is part of a broader investigation that will utilize velocity and species measurements to characterize the instantaneous interaction of the velocity and the relevant scalars, such as species and temperature, to understand turbulent flame behavior in a supersonic cavity combustor.

B. Background

A number of investigations employing planar laser-induced fluorescence (PLIF) of the OH, CH_2O, and NO radicals have been used to examine the instantaneous locations of the hot products, fuel consumption, and non-reacting fuel mixing behavior, respectively. A study by Gruber *et al.* [2] utilized NO PLIF to visualize fuel distribution and mixing and OH PLIF to visualize the distribution of the combustion products for various injection strategies. They found direct cavity injection from the downstream ramp produced the best fuel mixing and most robust combustion, both at nominal conditions and with increased back pressure characteristic of dual-mode scramjet performance. They also observed the development of unsteady combustion at low fuel flow rates. A later study by Rasmussen *et al.* [1] used OH and CH_2O PLIF to visualize the flame-holding mechanisms in a cavity combustor with varied fuel injection locations and flows with a Mach 2.4 main duct flow. They found that the local flame stabilization behavior had a strong dependence on the location and quantity of the fuel flow for both the floor and the downstream step. In general, lower fuel flow rates resulted in more combustion at the upstream shear layer between the primary recirculation zone and bulk flow, which was piloted by hot combustion products in the secondary recirculation zone. Increasing the fuel flow eventually quenched the combustion at the upstream of shear layer and shifted combustion downstream, where it stabilized in both the shear layer and primary recirculation zone.

American Institute of Aeronautics and Astronautics

Though OH and CH$_2$O PLIF provide insight into the combustion behavior, the turbulent flame behavior is inherently coupled to the cavity, shear layer, and free-stream velocity field and the associated transport of momentum, heat, radicals, and fuel. Unfortunately, instantaneous velocity measurement in general and particle image velocimetry (PIV) in particular are challenging due to large velocity gradients across shear layers and large variation in velocity ranges across the field of interest. Shear layers present problems because the seed particle needs to change velocity (direction and magnitude) with a time scale comparable to the flow to capture the flow dynamics accurately. This may be mitigated by using ever-smaller particles, but if the particle is too small, then the resulting small laser scattering magnitude will compromise detection of the particle, resulting in a weak signal in comparison to the background. Particulates also have tendency to cling to one another, or agglomerate, and to surfaces, obscuring windows, as static charges build up across the particles through collisions with other particles and surfaces. A particle cluster, with a larger combined mass but smaller mass-specific drag has a larger response time to changes in velocity. Additionally, the larger mass creates larger forces when the cluster collides with surfaces, and the potential for abrading windows is thus greater. Particle image velocimetry (PIV) measurements of isothermal, supersonic cavities may be found in the literature [10], but PIV measurements in reacting flows have been rare. An exception is the work by Scheel, where stereoscopic PIV was used in a small geometry with seeding in both the air and the hydrogen fuel, allowing scattering from particles across the flow domain [5]. Scheel's study reveals that seeding supersonic flows requires careful consideration of the flow and geometry to engineer the seed delivery to the region of interest.

The principal issue with PIV in reacting flow is the decrease in gas density with combustion, which likewise decreases the seed density of the hot products, making velocity calculations from the images problematic at some locations in the domain. In premixed flames and with careful control of the seed density, this abrupt change in seed density may be used to estimate the location of the flame contour, but with turbulent or non-premixed combustion, this approach may not be used as accurately.

II. Experimental Description

A. Direct-Connect Supersonic Tunnel

Experiments were performed in the direct-connect supersonic research facility, described in detail in Refs. 2,4, and 11. A simple flow path profile is shown in Figure 2; the coordinates will be referred throughout this document. Continuously flowing air was directed through a plenum through an asymmetric nozzle designed for operation at Mach 2, followed by an isolator section 15.24 cm wide, 5.08 cm high, and 17.78 cm long. The air then passed through the test duct, with 2.5^o divergence at the floor, where the inclined trapezoidal cavity was located. The cavity extended the full width of the duct, with a 1.65 cm depth and a 4.65 cm length. The upstream step was angled at 90° while the trailing edge ramp was at angled at 22.5^o.
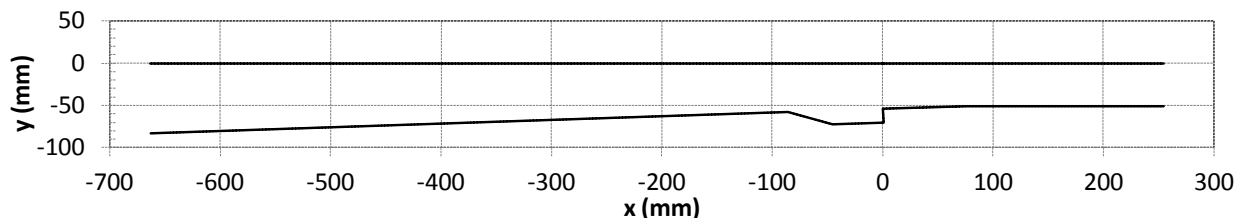
Figure 2: Flow path diagram, with coordinates matching subsequent figures.

Table 1 Rig conditions for the three flow regimes. SLPM refers to standard liters (referenced to 273 K and 1 standard atm) per minute

Case	1	2	3	4	5
T_o (K)	589	589	589	589	589
P_o (kPa)	483	483	483	483	483
Mach	2	2	2	2	2
U_∞	727	727	727	727	727
Fuel (SLPM)	0	56	99	39$\rightarrow$36	110

American Institute of Aeronautics and Astronautics

Figure 3: Diagram of heat release, combustion products, and fuel vapor with increasing fuel flow rates.

Tests were performed at the total pressures and temperatures shown in Table 1. The cases, designated as 1 through 5, were nominal isothermal (Case 1 in Table 1), *medium power* (Case 2), *medium-high* (Case 3), lean *blow off* (Case 4), and *high power* (Case 5), respectively, allowing us to compare velocity behavior of isothermal and four different reacting conditions with four levels of heat release.

Other studies have been performed with similar conditions and geometry that have revealed the time-averaged distribution of the flame and products within the cavity as fuel flow increased. OH PLIF measurements by Hsu *et al.* [4] were performed with the same geometry and similar fuel flows and revealed the time-averaged and standard deviation distribution of OH, a hot combustion product, across the same region of interest, as well as across three planes at different axial locations. Chemiluminescence imaging in a study of another trapezoidal cavity combustor by Lin *et al.* [12] and OH PLIF and CH_2O PLIF measurements by Rasmussen *et al.*[1] in a rectangular cavity combustor revealed how and where the fuel was consumed and burned. They found that as fuel flow rates increased from lean to high power, combustion shifted from stabilizing largely within the cavity, to the shear layer. The diagrams in Figure 3 show the approximate, time-averaged distribution of the heat release (red), combustion products (pink) and fuel vapor (grey). In the study by Hsu *et al.*[4], at low power fuel flow (~ 40 SLPM), the fuel burned within the cavity, creating a region of hot products in the low velocity regions at -50 mm $\leq$ x $\leq$ 0 mm.

As the fuel flow was increased to medium power rates (~50 SLPM), which corresponds to conditions near Case 2, there were hot products within the length of the cavity, while the reaction shifted away from the ramp because of the increased mixing distance required to mix the fuel and air. At a fuel flow rate of ~60 SLPM, the OH started to disappear from the low velocity region in the cavity, while hot products, indicated by OH fluorescence, began to populate the shear layer mixing region and the ramp impingement zone. This suggested that as the cavity fuel concentration increased, it was sufficiently high to extinguish combustion within the cavity, near the upstream step. CH_2O PLIF measurements by Rasmussen *et al.* [1] indicate fuel was still consumed near the downstream fuel ports as fuel flow increased, a clear indication that cavity combustion was still occurring and able to pilot the more luminous shear layer flames that stabilized between the fuel rich cavity and the air of the bulk flow.

With an increase in the fuel flow to 96 SLPM, corresponding approximately to the medium-high power of Case 3, combustion products populated primarily the shear layer impingement zone and downstream while the shear layer flame shifted downstream from the separation point.

At high power, corresponding to Case 5, the bulk of the heat release was at the shear layer, though further downstream from the separation point than the medium-high conditions, and also above the ramp. As the fuel flow increased, the reaction zone shifted further downstream, as shown in High+ of Figure 3. In this state, the flames stabilized from products mixing upstream with the fuel in the cavity, and then mixing with air in the shear layer, until combustion stabilized.

The shift in stability from low to medium and higher fuel flow rates suggests a coupled stability regime with flame anchoring in two different regions of the flow. Near the fuel ports, weak combustion is anchored at the interfaces of the fuel jets and entrained air by combustion products from the shear layer. The resulting hot combustion products are then convected through the cavity and to the shear layer separation region, where they anchor the shear layer flames. Lean or rich blow off occurs when this dual-anchoring process breaks down. The study by Lin *et al.* [12] revealed that as the fuel flow began to approach the rich limit, the flames stabilized above the fuel injection site, at and downstream from the ramp stagnation zone. The cavity and shear layer became too

4

rich and cool for combustion, such that only at the local, low velocity region at the ramp could stabilize combustion. Without the piloting effect of shear layer combustion, the flames around the fuel jets were eventually extinguished. The study by Lin *et al.* also suggested that lean blow off occurred similarly, but without the effect of rich extinction in and adjacent to the cavity. Instead, with insufficient fuel to stabilize combustion in the shear layer, only the cavity products were recirculated back to the fuel port combustion region, but they were not sufficiently hot to anchor combustion.

The results from Hsu *et al.* [4] also revealed strong three-dimensionality in the time-averaged OH distribution for the *medium-high* fuel flow, with hot products non-uniformly distributed across the span of the shear layer. Given that fuel was injected uniformly across the span of the cavity, this would result from spanwise redistribution of the fuel and heat release, produced by secondary flow within the cavity.

B. Optical Diagnostics

PIV has been used in a number of different flows as a minimally invasive method to measure velocity. PIV in supersonic flows has a number of difficulties due to the high velocities and large velocity gradients. If the particle does not change velocity as readily as the continuum of the flow, the paired Mie-scattering images do not indicate the actual path of the flow. Particle-fluid interaction is frequently described by the Stokes number, which is the ratio of the particles' characteristic momentum time scale, τ_p, to that of the fluid, expressed by:

$$\text{Stk} = \tau_p \frac{U}{d} \tag{1}$$

where the U is some characteristic velocity and d is some characteristic length, whose ratio may be replaced by a spatial derivative [13]. If the Stokes number has a magnitude at or greater than one, then the particles' response time is greater than that of the fluid, and the calculated velocity is suspect. Results from an investigation of a supersonic shear layer by Urban and Mungal showed that the particle size and density need to be minimized in order to optimize flow responsiveness, allowing the seed particle to cross the shear layer [14]. Otherwise, the momentum of the particle will introduce a streamwise velocity bias to the calculated velocities at the shear layer. The seed responsiveness to the flow continuum may be calculated by the expression described by Erbland [15]:

$$\tau_p = \frac{\rho_p d_p}{18\mu_g}\left[1 + \text{Kn}\left(2.492 + 0.84e^{-\frac{0.435}{\text{Kn}}}\right)\right] \tag{2}$$

Where d_p is the particle diameter, ρ_p is the particle density, μ_g is the dynamic viscosity of the fluid, and Kn is the Knudsen number of the particle and the gas, the ratio of the mean free path and the particle radius, and accounts for the Brownian motion of the seed particle as it collides with molecules in the gas.

Though the seed responsiveness may be improved with decreasing diameter, if the particle diameter is too small with respect to the laser wavelength, the scattering from the particle becomes too small in comparison to the background signal (which can arise from scattering from surfaces and flame emission), and the signal-to-noise ratio (S/N) becomes too small for accurate velocity calculation. In this investigation, the primary seed was a polydispersive mixture of spherical TiO_2 (anatase) particles with a nominal particle size of 100 nm, supplied by American Elements. The small diameter insured that the particles would follow the flow, while they were large enough to provide scattering with an acceptable S/N.

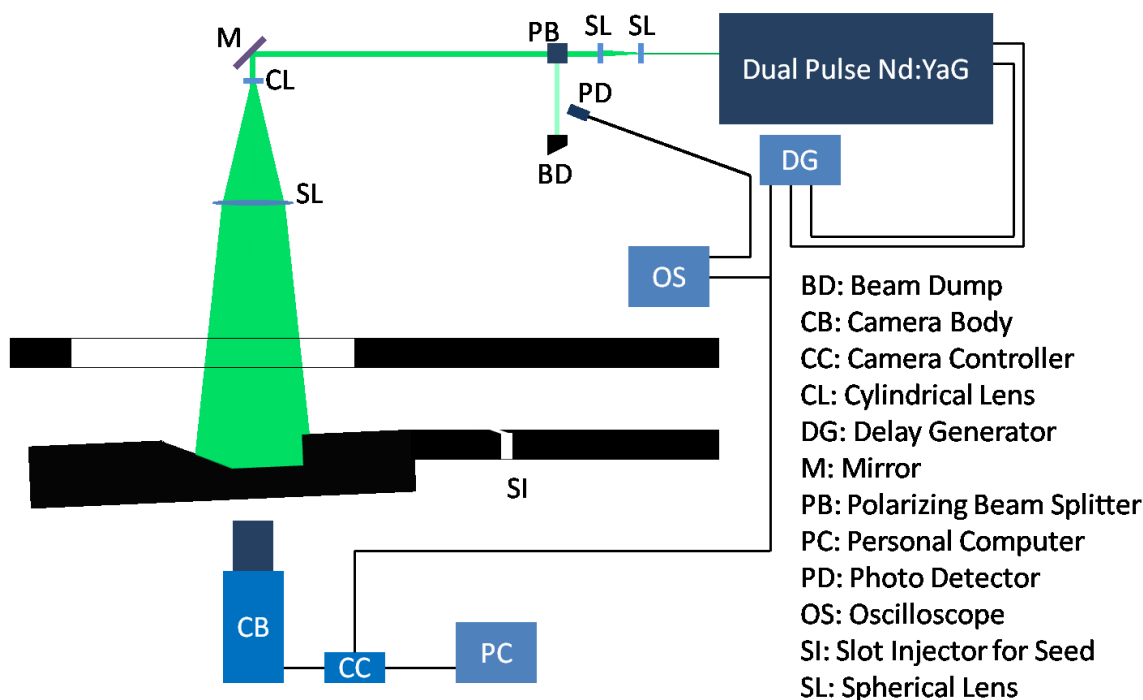**Table 2 PIV seed characteristics[16,17,18].**

Compound	Name	Mohs	ρ_p (kg/m^3)	T_{melt} (K)	n_ε	κ_e
Al_2O_3	Alumina	9	3960	2327	1.8	9.9
TiO_2	Anatase	5.5	4230	2098	2.5	110
TiO_2	Rutile	6	4250	2128	2.6	173
SiO_2	Silica	7	2600	2003	1.5	4.2
ZrO_2	Zirconia	8	5680	2988	2.2	12.5

TiO_2, in the anatase form, was chosen over other available compounds in order to address potential issues with both the experimental hardware and optical behavior. It has a much lower hardness (Mohs), greater index of refraction (n_ε) and dielectric constant (κ_e), than other potential seed material (e.g., Al_2O_3, a widely used seed material). The lower hardness minimized the abrasion of the windows, while the high dielectric constant ensured

American Institute of Aeronautics and Astronautics

that static charges accumulated during entrainment and transport did not dissipate, keeping particles separated. Contact with grounded surfaces, such as the metal tubing and walls would have readily dissipated any charges, reducing wall agglomeration. Agglomeration obscures windows and forms cluster of particles that produce CCD-saturating scattering and respond poorly to changes in the flow continuum.

The optical set up used for this investigation is shown in Figure 4. The camera body (CB), a Cooke Corp. PCO 1600, was controlled by the camera controller (CC) via a personal computer (PC). A trigger signal was sent from the camera controller to a Stanford Research Systems DG535 delay generator (DG), from which the Q-switches of the two laser heads in of the New Wave Solo were individually triggered with a 2.2 μs time step, Δt. In this way, the laser's pulse repetition rate was dictated by the camera's framing rate; for the measurements shown here, the framing rate and pulse repetition rate were about 30 Hz and 425 pairs of images were collected for each condition. The beam exited the laser, as shown in Figure 4, passed through a two-lens telescope to enlarge the beam and reduce the laser intensity before passing through the polarizing beam splitter (PB) used to adjust the laser intensity directed to the interrogation volume. The beam was then directed through a cylindrical lens to expand the beam to a sheet and then another spherical lens to narrow both the breadth and thickness of the sheet to form an interrogation volume that fit within the cavity length with a thickness of 0.5 mm. The diverted laser light from the polarizing beam splitter was directed to a beam dump (BD). Scattering from the edge of the beam dump cavity was gathered by a photodiode (PD). The resulting PD signal, along with the with the camera trigger signal, was directed to an oscilloscope to measure the actual time step. The TiO_2 seed particles were entrained by air in an Innovative Scientific Solutions, Inc. vibrating cyclone aerosol generator and then directed through the angled seed injection (SI) slot jet placed in the isolator wall. The flow rate of seeded air from the slot injector was small, about 10 SLPM, to ensure minimal disturbance to the flow but allow a centrally seeded region of the flow.

Scattering was collected with a Nikon 60-mm focal length macro lens fitted with a 3-nm (FWHM) bandpass filter to suppress strong flame emission; the lens f-stop was set to f/8. Spatial calibration was performed by imaging a block gridded with horizontal and vertical lines spaced by 3.175 mm. Across the image plane, the mean pixel resolution in both the horizontal and vertical directions was 5.6612×10^{-5} m/pixel, with an uncertainty, based on a 95% confidence level, of 1.4784×10^{-8} m/pixel, or 0.0261%.

Figure 4: Diagram of the optical set up used in this investigation.

BD: Beam Dump
CB: Camera Body
CC: Camera Controller
CL: Cylindrical Lens
DG: Delay Generator
M: Mirror
PB: Polarizing Beam Splitter
PC: Personal Computer
PD: Photo Detector
OS: Oscilloscope
SI: Slot Injector for Seed
SL: Spherical Lens

Calculation of the velocity fields for each pair of images was performed with DaVis FlowMaster 7.2. Images were imported, calibrated geometrically, paired, and then temporal attributes were added. For each image, a sliding background, or high-pass filter, with a 10 pixel scale length was applied to minimize background non-uniformities.

American Institute of Aeronautics and Astronautics

Regions of the image that were irrelevant or had poor seeding were masked to minimize computational time. A cross-correlation calculation approach was used, with standard FFT calculation and Whitaker reconstruction of the final result. Iterative multi-pass calculation, stepwise resolution increases, and integer window shift were implemented. Twenty passes were made at each window size to ensure that the calculations had converged upon the best fit to the data. Interrogation window sizes were decreased from 128x128 to 32x32 pixel^2, with 50% window overlap, giving a vector spacing of 9.06×10^{-4} m/vector but a spatial resolution of 1.81×10^{-3} m. Integer window shift was allowed up to 32 pixels, allowing velocity resolution to 32x32 pixels with reliable seed pixel shifts across the domain to capture the highest velocities. Vectors were deleted if their cross correlation Q-ratio was less than 1.1, with a single pass 3x3 smoothing. Details of the theories behind these methods are discussed in Refs. 19 and 20.

A number of velocity-based quantities were also calculated to understand both the fluid strain and rotation. From the two-dimensional stress tensor, $\frac{\partial U_i}{\partial x_j}$, the symmetric and antisymmetric elements may be separated, forming the respective expressions:

$$\frac{\partial U_i}{\partial x_j} = \begin{bmatrix} \frac{\partial U}{\partial x} & \frac{1}{2}\left(\frac{\partial U}{\partial y}+\frac{\partial V}{\partial x}\right) \\ \frac{1}{2}\left(\frac{\partial V}{\partial x}+\frac{\partial U}{\partial y}\right) & \frac{\partial V}{\partial y} \end{bmatrix} + \begin{bmatrix} 0 & \frac{1}{2}\left(\frac{\partial V}{\partial x}-\frac{\partial U}{\partial y}\right) \\ \frac{1}{2}\left(\frac{\partial U}{\partial y}-\frac{\partial V}{\partial x}\right) & 0 \end{bmatrix} \tag{3}$$

where the first matrix on the right hand side, S_{ij}, is the two dimensional strain rate tensor, containing the normal and shear strain rates that describe fluid element deformation, and the second matrix contains the non-deforming rotational elements, or one half of the z-vorticity [21]. Directions and velocity notation is shown in Figure 1. For most of the domain, velocity gradients were calculated using the fourth order central difference scheme known as the Richardson Extrapolation [19] within Matlab. A first-order differencing scheme, forwards or backwards depending on the location, was used at the edges of the velocity domain, while just inside of the edge cells a second order central differencing scheme was used. Given the non-uniform seeding distribution, there were occasional locations within the domains without valid vectors. These were treated as domain edges to minimize erroneous gradient values. From the symmetric tensor, the principal strains and their directions were calculated using the matrix eigen solver within Matlab.

To characterize the turbulent behavior of the flow field, the time-averaged stream-wise velocity (U), in-plane cross-stream velocity (V), velocity magnitude (|U|), out-of-plane vorticity ($\bar{\omega}_z$), and Reynolds stresses ($\overline{u'u'}$, $\overline{v'v'}$, $\overline{u'v'}$) were calculated from the series of velocity fields for each case.
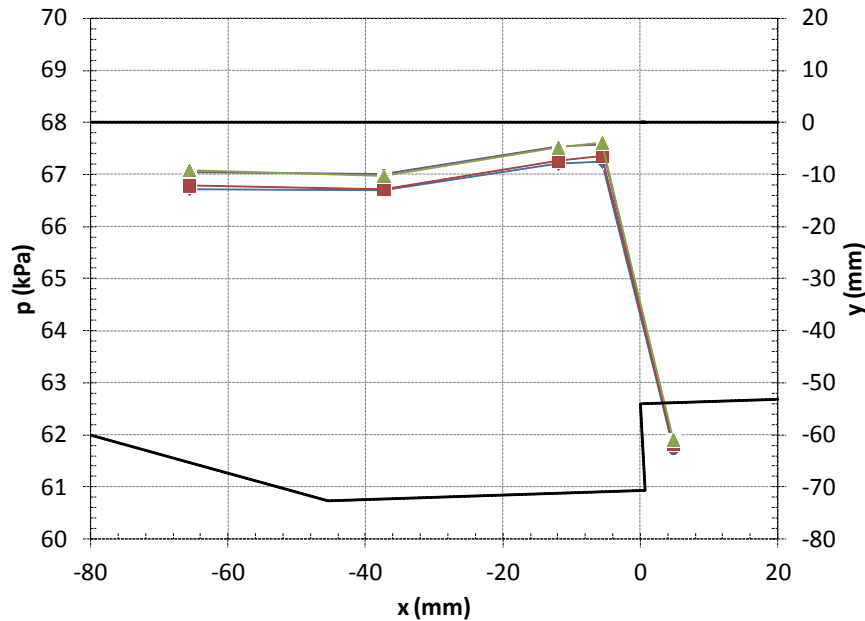
Figure 5: Cavity surface static pressure profile measured along the bottom surface of the rig. (◆) No seed, no flame, (●) seeded flame, (■) no seed, no flame, (▲) seeded, no flame, (—) tunnel surface.

III. Results

The influence of the seeding flow on the surface static pressure may be seen in Figure 5 for Cases 1 and 3. There was a maximum shift of 0.31 kPa, which corresponds to a shift of 0.11%. From the small shift in surface pressure, we may assume that the influence of the slot injector on the cavity and shear layer flow was minimal and that the flow behavior we measured with PIV was the same as that without the seeding flow.

Examples of instantaneous and time-averaged results from the representative cases are shown in the following sections. Instantaneous, isothermal results will be shown and discussed first in Section A, followed by the instantaneous results from reacting flow in Section B. Section C will compare the time-averaged isothermal and reacting velocity results shown in Sections A and B, as well as discuss velocity-derived values such as the vorticity, Reynolds stresses, and principal stresses.

A. Isothermal

A typical instantaneous velocity field is shown in Figure 6 for Case 1. Flow was right to left, with the upstream cavity step at y ~ -10 mm and the downstream ramp step at y ~ -13 mm. There was an approximately 1.5 mm gap between the edge of the boundary shown in the plot and the actual surface of the cavity. The edges marked where thin plates were used to mask the camera from the laser scattering from the cavity surface, which is considerably greater than the scattering from the PIV seed particles. Figure 6a reveals very little variation in the Mach 2 bulk flow across the length of the cavity, though the vectors within the cavity recirculation zone are too small within the figure to make their direction discernible.

The particle trace image in Figure 6b reveals a great deal more about the instantaneous direction and paths of the flow within the cavity and across the shear layer. It should be noted that these are not streamlines, which are representative of the mass conservative stream function. Instead, a sparse distribution of the vector points was chosen, and path lines were calculated from those locations to form particle traces, which were then colored by the two-dimensional magnitude.

There are a number of behaviors that may be observed from the particle traces in Figure 6b. First, the traces of the instantaneous velocity field show that the cavity flow is much slower in comparison to the bulk flow above the shear layer, which is to be expected for a separated flow. The reader will notice that some particle traces are to or from outside of the masked boundaries, implying in the some parts of the geometry, significant flow could not be measured properly with PIV. There are a number of regions where the path lines converge or diverge, indicating out-of-plane sinks or sources, such as can be seen at x~-25 mm, y ~ -60 mm. These convergent/divergent regions are observable in all of the instantaneous particle trace plots, revealing that the cavity flow exhibits typical, three-dimensional flow behavior expected from fully turbulent flow, even with the two-dimensional geometry.

A number of eddies are discernible in the particle trace plot in Figure 6b, particularly at x ~ -50 mm and y ~ 62 mm. These eddies were observed in all of the instantaneous images and, though they appeared to be distributed randomly within the cavity, there was usually one observed adjacent to where the shear layer impinged against the downstream cavity ramp, forming a stagnation zone. Like the size, shape and location of the cavity eddies, the location of the shear layer impingement against the ramp also tended to vary in location. The consistent appearance of the principal eddy adjacent to the shear layer impingement or stagnation point suggests that these two processes were coupled. Since each frame was independent of the other, there was no indication if the eddy structures were formed by the shear layer at the upstream step and then were convected downstream, or if they were formed by the shear layer stagnation and then convected upstream, or if both processes occurred, coupled or uncoupled.

In previous studies of cavities, with perpendicular walls, researchers were able to demonstrate coupled behavior of the shear layer separation with the generation and propagation of acoustic perturbations at the downstream wall, which coupled with the upstream shear layer roll up as well as with any turbulent heat release within the cavity. One of the earliest empirical models, developed by Rossiter [22], related acoustic oscillation frequency, cavity length, free-stream velocity, and a number of empirical constants. Later studies were able to demonstrate coupled behavior of the shear layer separation with the generation and propagation of acoustic perturbations at the downstream wall, which coupled with the upstream shear layer roll up as well as with any turbulent heat release within the cavity, as discussed in the review by Rowley [23]. With the downstream wall of the cavity at an acute angle to the flow, the dynamic relationship between the upstream shear layer separation becomes more stable [24].
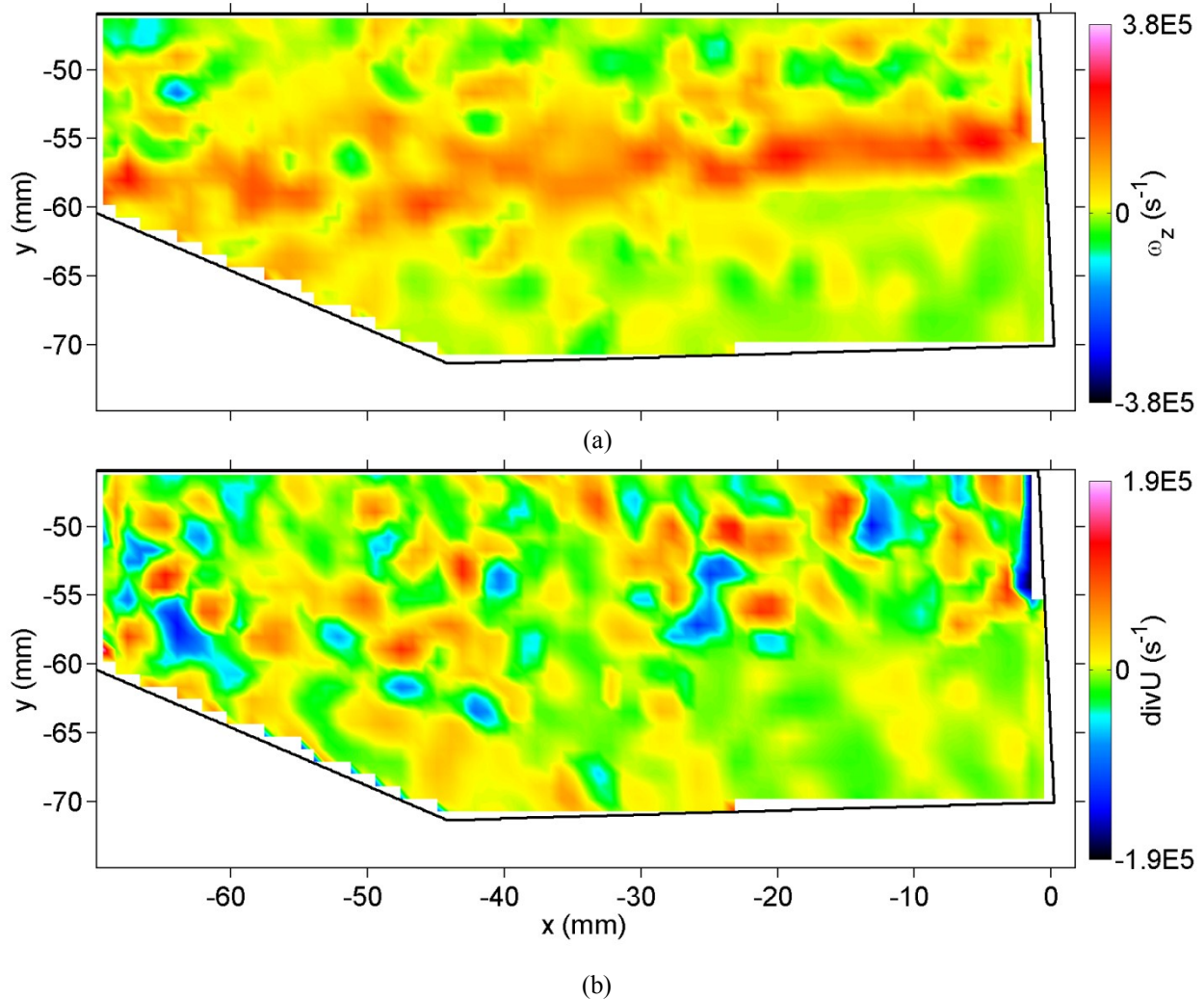
Since the high-momentum bulk flow is on one side of the shear layer, the cavity on the other, and the shear layer impinges against the downstream ramp, the flow is reminiscent of a confined impinging jet. Impinging flows have been examined not only because of their high heat transfer rates, but also because of their globally unstable behavior

American Institute of Aeronautics and Astronautics
Approved for public release; distribution unlimited

[25]. A global instability in a flow field is characterized by its oscillatory influence it exerts on the flow, producing fluctuations that propagate throughout the domain of the flow, while a convective instability is characterized by the amplification of an existing fluctuation to higher amplitudes and the subsequent transport of that fluctuation [26]. Given the similarity of the impinging shear layer to that of the impinging jet and previous cavity studies, similar globally unstable behavior is likely, but time-resolved investigations are necessary to reveal the dynamics of the associated velocity field.
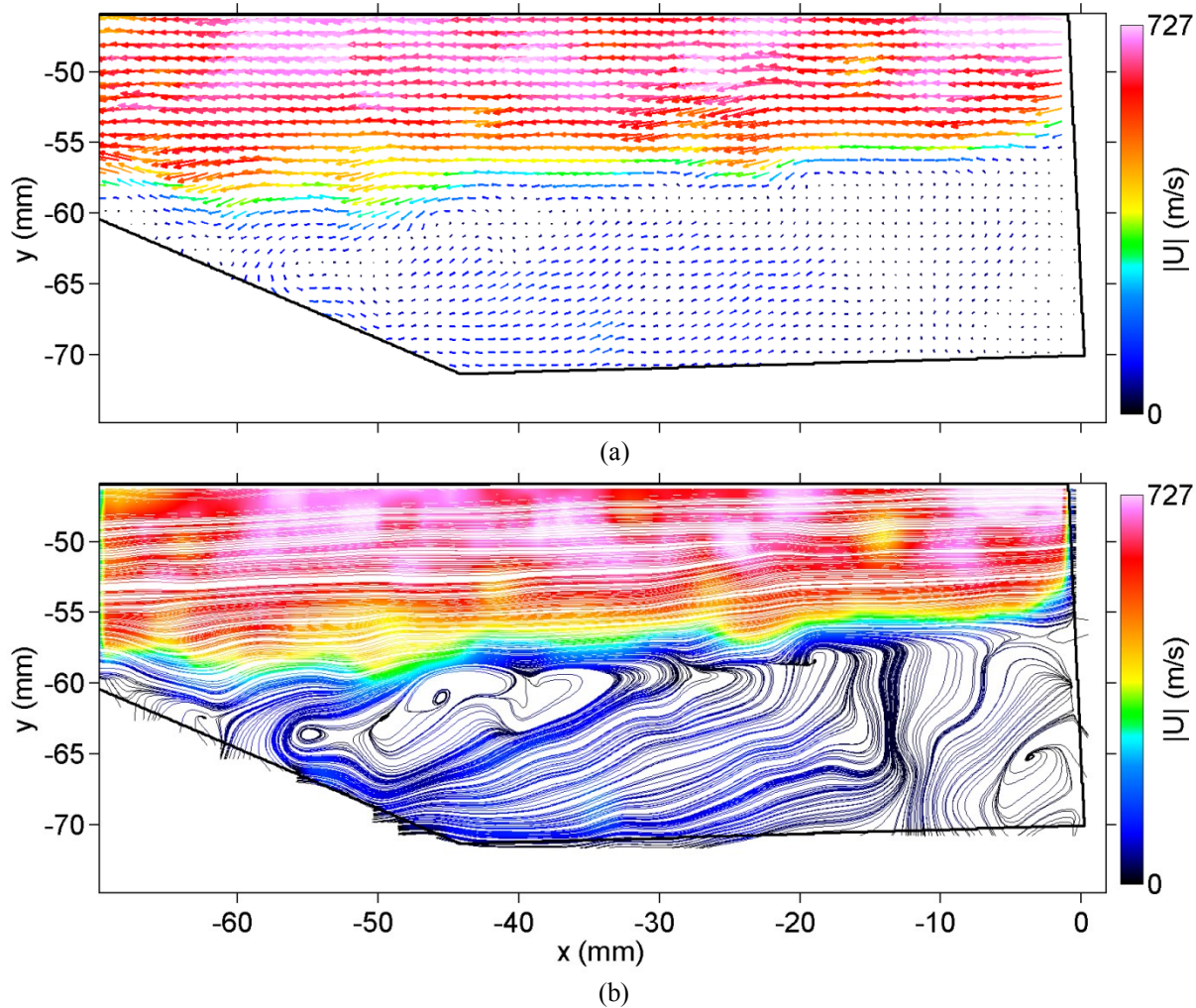
Figure 6: Instantaneous velocity field vectors colored by velocity magnitude (a) and particle traces (b) at isothermal conditions, Case 1, across cavity, shear layer, and section of bulk flow.

A careful examination of Figure 6b reveals the presence of a secondary eddy structure, centered at x ~ -5 mm and y ~ -65 mm, rotating in the opposite direction of the primary eddy structure formed by shear layer impingement. The presence of this structure was predicted computationally in Ref. 24, but the morphology and presence in the flow is unsteady and indeterminate. This and other particle trace plots reveal a flow field that is unsteady, three-dimensional, and very different than the time-averaged flow field that may be calculated with RANS.

American Institute of Aeronautics and Astronautics
Approved for public release; distribution unlimited

(a)

(b)

Figure 7: Instantaneous vorticity (a) and two-dimensional divergence (b) at isothermal conditions, Case 1, across cavity, shear layer, and section of bulk flow.

Figure 7a shows the vorticity contours calculated for the same velocity field shown in Figure 6. Shades of orange, red and pink are positive vorticity, while shades of green to dark blue are negative vorticity. Considering the direction of the flow, the predominant vorticity values are positive, with the greatest positive values indicating where the shear layer was located. The shear layer appears to exhibit the randomness and broadband length scales of a local, convective instability [27]. Where the shear layer impinged against the downstream ramp, we see a wide region of relatively large positive vorticity as the eddy structures were formed. Within the cavity, the vorticity contours indicate smaller values and gradients, a result that can be attributed to the lower velocities than found in the rest of the flow field.

The plot in Figure 7b shows the divergence of the two-dimensional velocity. Considering the subsonic velocity in the cavity and the near constant Mach number in the free-stream, the three-dimensional divergence of the velocity should be small. The two-dimensional divergence shows the approximate distribution of the negative out-of-plane velocity gradient, $-dW/dz$. A careful examination of the magnitudes indicates peak values nearly half of the vorticity limits within the region of the bulk flow, while within the cavity the magnitude range is narrower. If we recall the particle trace plot in Figure 7b, we realize that we are neglecting a great deal of the flow behavior by only considering two-dimensions. In order to characterize the out-of-plane velocities, stereoscopic PIV would need to be used, while tomographic PIV would resolve both the velocity and the velocity gradient.

American Institute of Aeronautics and Astronautics
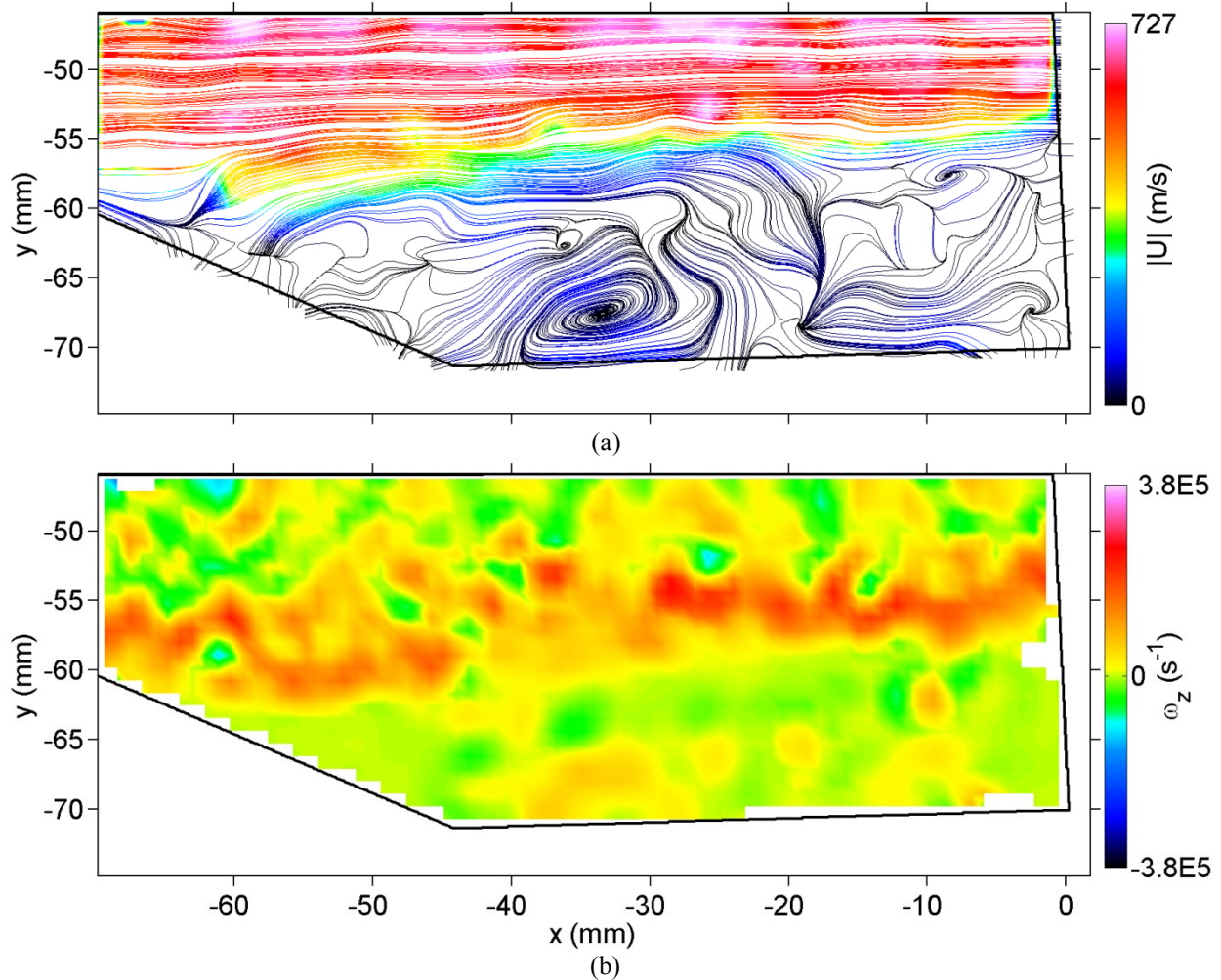
Figure 8: Instantaneous particle traces colored by velocity magnitude (a) and vorticity contours (b) at reacting conditions, Case 3, across cavity, shear layer, and section of bulk flow.

B. Reacting

A typical instantaneous particle trace field and vorticity contours are shown in Figure 8 for reacting conditions corresponding to Case 3, the *medium-high* power reacting conditions. Again, the velocity field in Figure 8a changed little in magnitude or direction above the shear layer, approaching ideal bulk flow velocity of Mach 2, or 727 m/s. Comparing with Figure 6a and b, the shear layer just aft of the upstream step appears to have thickened, a process typical of shear layers in reacting flows as the velocity gradient is dampened out by volumetric expansion and baroclinic torque [28]. The rest of the shear layer is not discernibly different from what may be observed in Figure 6a and b.

The particle trace plot in Figure 8a reveals much greater out-of-plane motion, with a path line convergence at 20 mm < x < 30 mm and -20 mm < y < -15 mm and path line divergence at x ~ 65 mm and -20 mm < y < -15 mm. These path line convergent/divergent regions indicate much stronger three-dimensional motion. There are still a number of eddies of varying sizes across the plane, but they are not as large or as clearly dependent on the impingement of the shear layer on the downstream ramp. Instead, the addition of heat release has appeared to add stronger out-of-plane motion, and from the presence of the convergent/divergent region, there may be an eddy structure with appreciable ω_x and ω_y.

The change in the shear layer impingement behavior may be further understood by comparing the vorticity contour plot in Figure 8b and Figure 7a. At isothermal conditions, the high vorticity values are spread out over a large area adjacent to the ramp, while the instantaneous vorticity contour plot for Case 3 shows a more distinct region of higher vorticity. Though this may be attributed to the instantaneous nature of the respective velocity

American Institute of Aeronautics and Astronautics

fields, the mean results in Section C will show that these instantaneous plots are representative of the mean behavior. These observations imply that heat release modifies the shear layer impingement and the formation of the recirculation zone eddy structures. The instantaneous mechanics of this behavior is not clear from the set of images gathered in this study because the relevant time scales are more rapid than can be gathered at 10 Hz.

C. Comparison

This section will show both velocity profiles and contour plots to compare the time-average results. The profiles provide a more precise, but less global, means of comparison, while contour plots provide a more global view of the morphology of flow features, but with less precision. The locations of the profiles are shown in Figure 9 for reference.
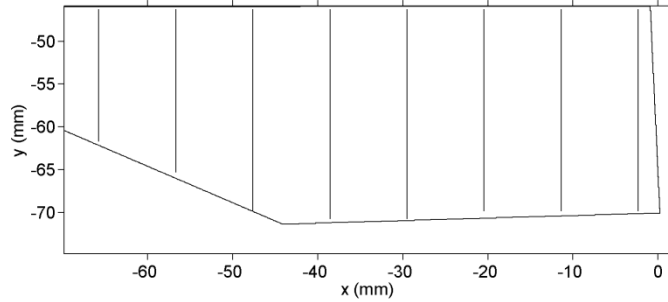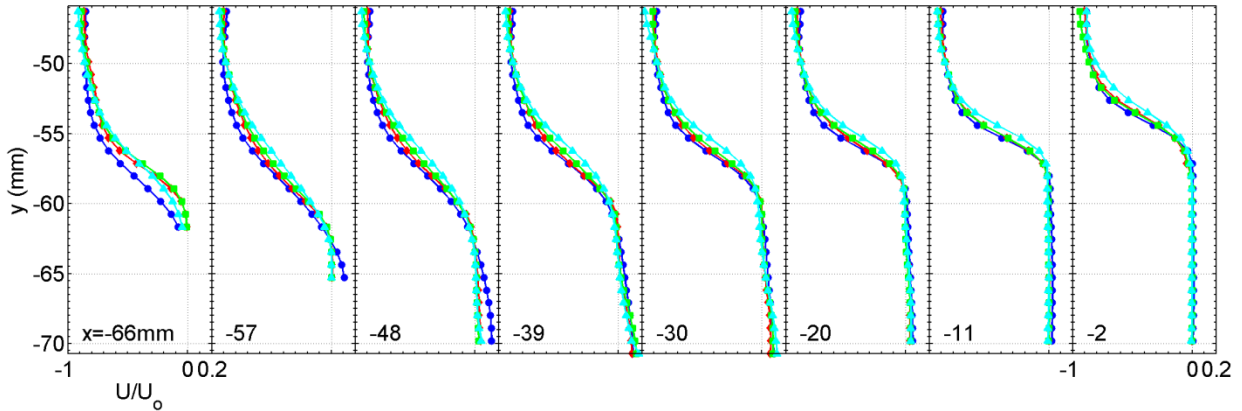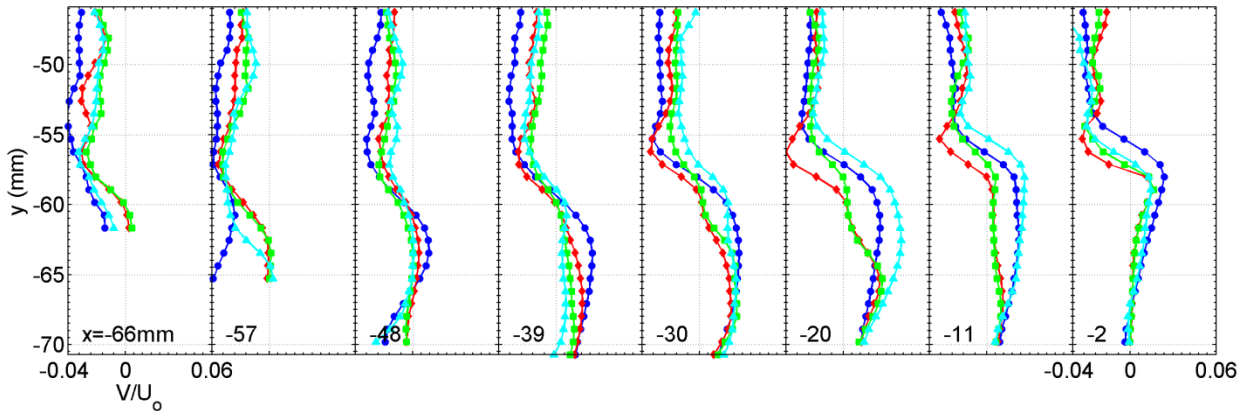

Figure 9: Profile locations in the domain.

(a)

(b)

Figure 10: Profile plots of averaged U (a) and V (b), calculated from 425 samples, for Cases 1 (●), 2 (♦), 3 (■), and 5 (▲).

American Institute of Aeronautics and Astronautics
Approved for public release; distribution unlimited

Figure 10 shows velocity profiles for Cases 1, 2, 3 and 5, with different symbols for each. The isothermal velocity profile stands out among all of the profiles, particularly downstream. Furthermore, identifiable trends may be observed. For simplicity, the profiles of U and V shown in Figure 10 have been normalized by the free-stream velocity, U_o=727 m/s.

The bottom of the profiles at x=-66, -57, and -48 mm indicate the shear layer impingement and stagnation zone by near-zero velocities. For the non-reacting case, the zero transition occurred between x ~ -66 and -57 mm, while for the reacting cases it is extended between x ~ -66 and -48 mm, a much longer region of the cavity ramp. This suggests that heat release has axially broadened the average, shear layer impingement region, either by shear layer thickening or by increasing the range of motion of the shear layer. Since these are averaged profiles, the unsteadiness of the stagnation regions will be discussed later to determine if the combustion attenuated or amplified the shear layer impingement instability; the average of both shear layer thickening and greater shear layer motion may appear similar along the ramp.

From x=-39 mm and upstream, the axial velocity profiles below the shear layer are indistinguishable from one another, suggesting that within the cavity, combustion modifies the axial flow at the ramp, but not within the rest of the cavity. The velocity gradient, characteristic of the shear layer, is gradually attenuated with distance from the separation at the upstream step and with increasing fuel flow rate. With Case 5, the highest fuel rate, the shear layer also appears to have shifted upward. During stable combustion, flames were observed at the downstream ramp where the fuel was injected and along the length of the shear layer. At the cavity ramp, the local heat release would have altered the flow by volumetric expansion while the shear layer velocity gradient would have been attenuated by a combination of dilatation, baroclinic torque, and increased viscosity [7,8].

The profiles in Figure 10b reveal that combustion and the amount of fuel flow altered the cross-stream velocity, V, in more complex ways than was observed in Figure 10a. Above the shear layer, we can observe a decrease in the downward velocity with increasing heat release and distance from the upstream separation, attributable to the volumetric expansion in the cavity from combustion. In the region of the shear layer, there were shifts in the velocity that were not directly proportional with fuel flow. At x = -30, -20, -11, and -2 mm and y ~ -55 mm, we can see that V is much less than either the isothermal or the *medium-high* and *high* power conditions. Within the cavity, the V profiles show strong dependence on the heat release, but as with other changes observed in the velocity behavior, without a clear view of the time-averaged heat release, it is difficult to understand what is driving the changes. The study by Rasmussen *et al.* [1] of a rectangular cavity showed that both the fuel consumption and the recirculation of hot products within the cavity shifted from lean, moderate, and rich fueling regimes. Judging from what we can observe in the V profiles, we can see similar dramatic shifts in the velocity.

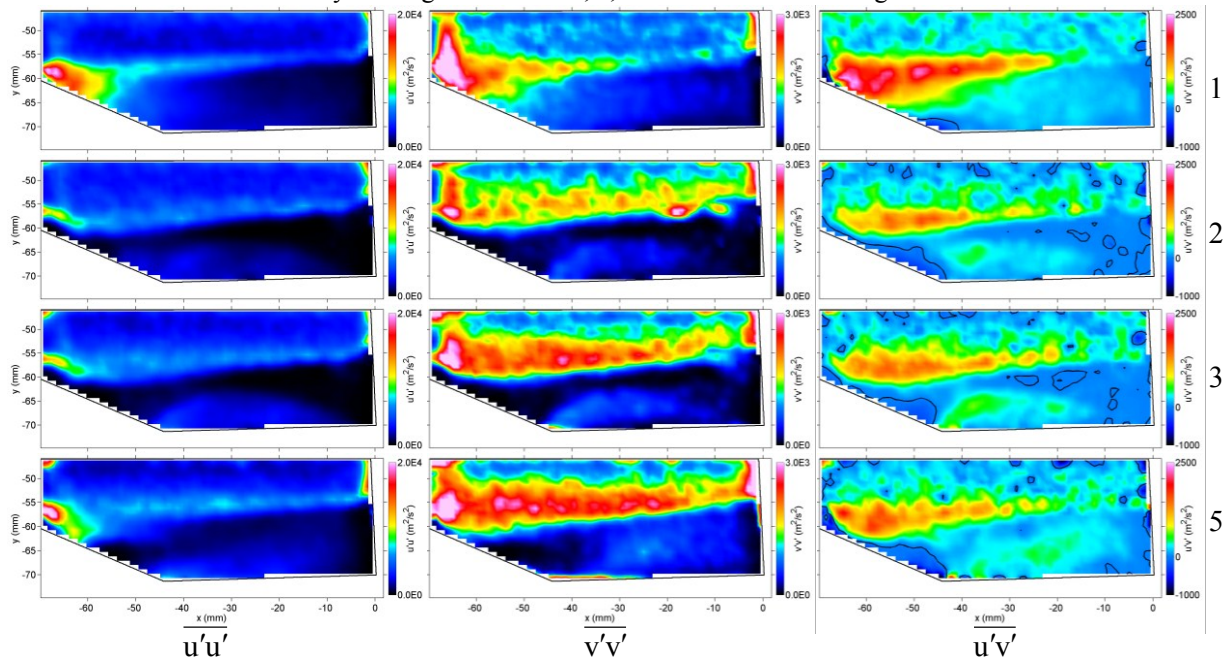An array of images for Cases 1, 2, 3 and 5 are shown in Figure 11 and

Figure 12 for comparison of time-averaged values as well as the variance and covariance statistical values that compose the time-averaged Reynolds stresses. The particle traces of the averaged velocity fields are plotted in the first column of Figure 11, with the contours of the averaged axial velocity, U, and cross-stream velocity, V, plotted in the center and right columns, respectively. Black zero-velocity contours call attention to the regions where the axial or cross-stream velocities change directions.

The particle traces of the averaged velocity field vary significantly between the difference cases. The isothermal particle traces appear to represent two-dimensional flow at the center plane of the cavity. A computational study by Freeborn et al.[29], using a κ-ω Reynolds-Averaged Navier-Stokes model, predicted two-dimensionality at the center plane of the cavity, with the formation of twin recirculation eddies on either side at the cavity ramp. The computational results, inherently time-averaged, compare well with the averaged results, but the unsteady measurements suggest that the eddy structures that extend across the width of the channel are as dynamic as the eddy structure that extends the height. Generally, unsteady cavity CFD studies are concerned with axial dynamics[23], which are of no small concern, but the unsteady, three-dimensional behavior at the center plane observed in this investigation, that increased with heat release, suggests that unsteady computational tools would reveal a great deal about the flow field.

While the isothermal particle traces appear to represent a two-dimensional flow, for all of the reacting cases there was clear indication of significant out-of-plane motion, as can be seen from the convergent traces just downstream of the shear layer separation. For Case 5, with the *high-power* fuel flow, there were also divergent traces between the center of the primary eddy and the downstream ramp. These observations reinforce the hypothesis that heat release produces a more three-dimensional flow field in the cavity, but do not clarify the nature.

A careful examination of the particle traces, shaded by velocity magnitude, in Figure 11 reveal that the primary recirculation eddy remained with combustion, but the velocity magnitude within the cavity was comparatively smaller than without combustion. The slower velocities may be attributed to two processes, both influenced by combustion. First, the rate of entrainment into the cavity is tied to the velocity gradient, which is attenuated by heat release in the shear layer. A shallower velocity gradient across the shear layer will transport less momentum and mass into the cavity. An idea of the velocity gradient at the shear layer can be extracted from the curvature of the particle traces where they turn downstream from the cavity. Second, we can observe from the $\overline{U}=0$ contour in second column of Figure 11 that the angle between the ramp and the shear layer impingement decreased with increasing heat release. The downward shift in the angle of the $\overline{U}=0$ contour suggest that the momentum of the bulk flow tended to contain the combustion-driven dilatation within the cavity, thickening the shear layer while compressing and slowing the primary recirculation zone. This corresponds with the heat release diagram shown in Figure 3, which showed that greater portion of heat release that occurred above the ramp with increasing fuel flow. The influence of the shallower shear layer impingement angle can also be seen in the thicker boundary layer at the cavity exit for Cases 2, 3, and 5.

Shaded contours of the time-averaged V field are shown in the third column of plots in Figure 11. Again, the zero-V contour is black for contrast. Recalling the findings of Hsu et al.[4] and Rasmussen et al.[1], we can observe how at *medium* power (Case 2), the heat release at the cavity ramp extended the zero-V contour downstream. At the higher fuel rates, where there was not appreciable heat release at the cavity ramp, only the impingement of hot products, the zero-V contour of the shifted back upstream. Along the shear layer regions, we can observe how the increasing shear layer heat release pushed the zero-V contour upward.
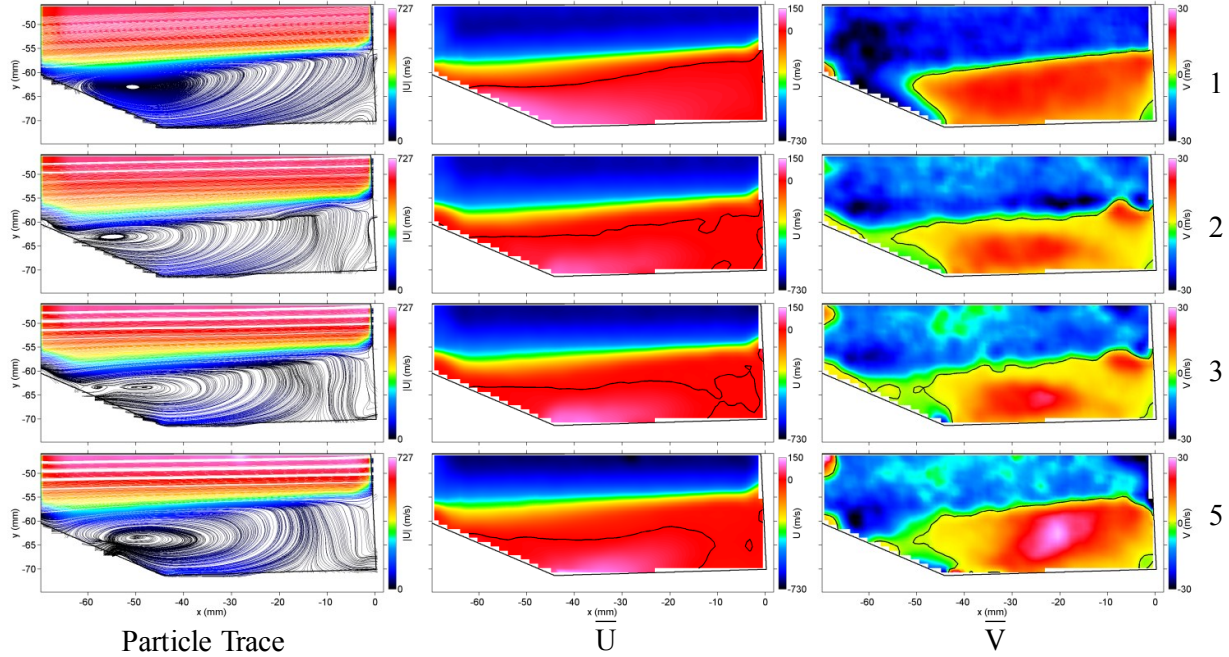
American Institute of Aeronautics and Astronautics
Approved for public release; distribution unlimited

Figure 11: Time-averaged values of the particle trace, U, and V.

We can observe from the particle traces, $\overline{U}$ contours, and $\overline{V}$ contours that the flow field strongly coupled to the both the amount and location of the heat release within the cavity and shear layer. Utilizing line-integrated chemiluminescence imaging may capture some of the behavior but without resolving the three-dimensionality of the flow and heat release. OH or CH_2O PLIF, gathered simultaneously with PIV, at various planes would reveal the location of hot products or fuel consumption, respectively, to create a much clearer picture of the coupled heat release and velocity.

The streamwise velocity variance, cross-stream velocity variance, and the covariance of both are shown in
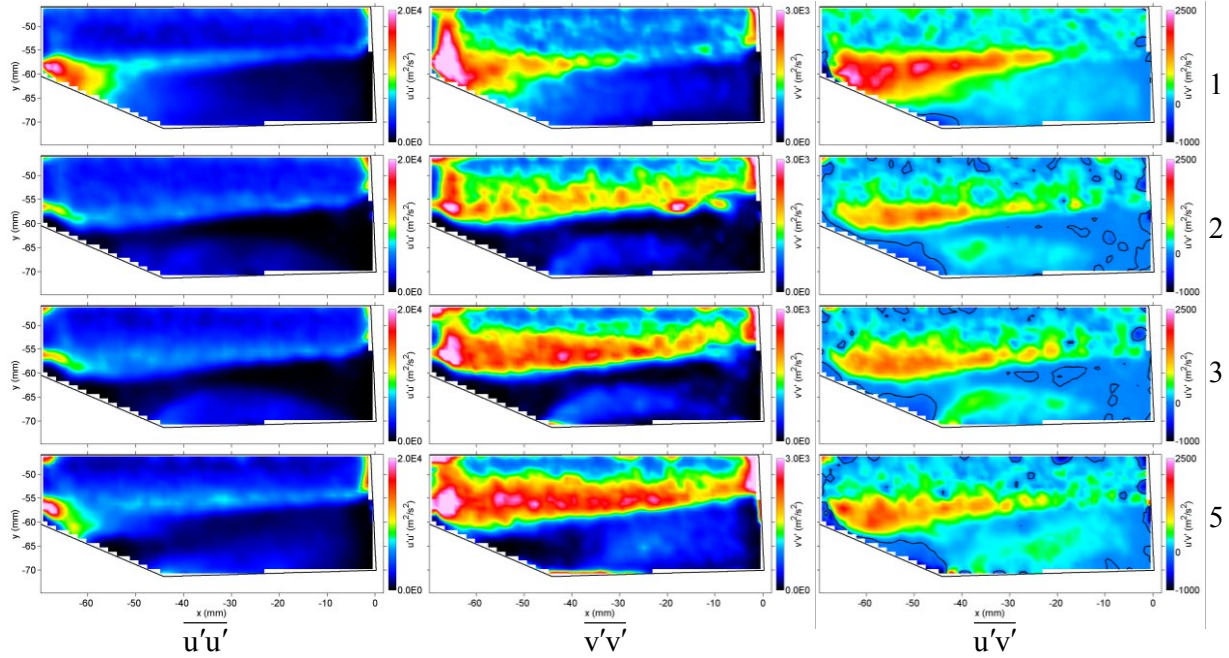

Figure 12 for Cases 1, 2, 3, and 5. In the non-reacting case shown in the first row, the unsteadiness at the shear layer impingement zone created the largest magnitude Reynolds stresses, while there were also appreciable magnitudes within the cavity. At the *medium* power fuel flow, the heat release along the length of the cavity

15

attenuated the cavity unsteadiness as well as along the shear layer and shear layer impingement zone. As combustion shifted downstream along the shear layer with increasing fuel flow, the shear layer unsteadiness increased, as well as that of the shear layer impingement zone, which suggest unsteady shear layer combustion. Furthermore, as combustion in the cavity reached the rich limit and was quenched, the cavity unsteadiness increased at the *high* power fuel flow of Case 5.

If we recall our discussion of the change in the shear layer impingement stagnation zone as observed from the axial velocity profiles in Figure 10, there was uncertainty whether the expanded stagnation zone was due to actual broadening or fluctuations in the shear layer location. From

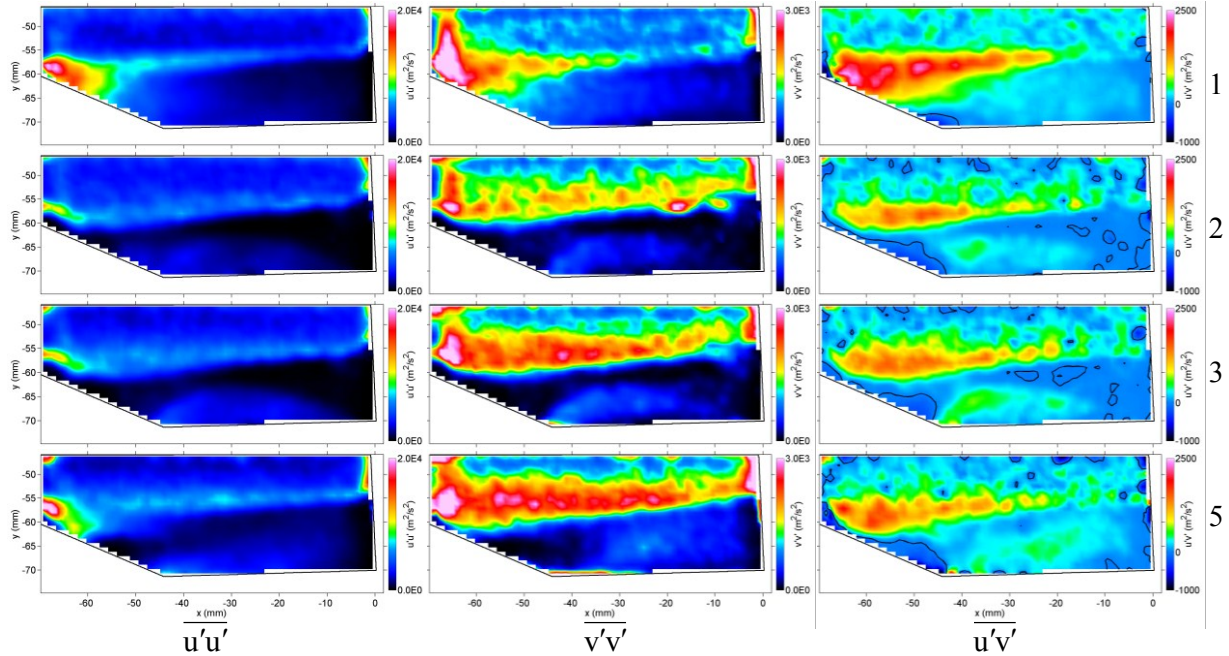$$\overline{u'u'} \qquad \overline{v'v'} \qquad \overline{u'v'}$$

Figure 12, we can see that the shear layer fluctuations at the stagnation zone decreased with heat release because of shear layer thickening and the attenuation of shear layer instabilities by combustion.
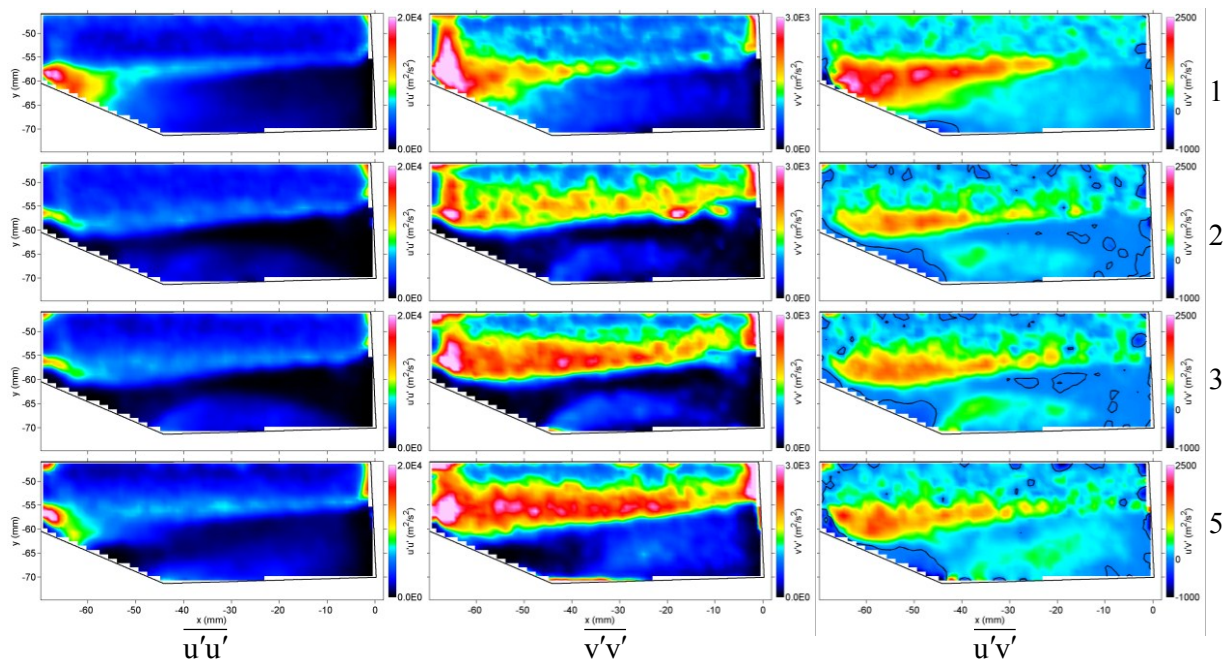

$$\overline{u'u'} \qquad \overline{v'v'} \qquad \overline{u'v'}$$

Figure 12: Time-averaged values of $\overline{u'u'}$, $\overline{v'v'}$, and $\overline{u'v'}$.

American Institute of Aeronautics and Astronautics

Recalling the work from Hsu *et al*. [4], as the fuel flow increased the combustion product unsteadiness at the shear layer increased as well but not in a way that was clearly discernible between cases. The work by Rasmussen *et al*.[1] reported time-averaged OH PLIF values but not of CH_2O nor the standard deviation or variance of either. CH_2O is a short-lived intermediate combustion species formed during hydrocarbon consumption and is present over a wide range of temperatures and is a good indicator of where the fuel is being consumed though not necessarily of the reaction zone [30]. A standard deviation value of CH_2O PLIF would provide a qualitative view of the reaction unsteadiness and may explain some of the velocity unsteadiness shown in
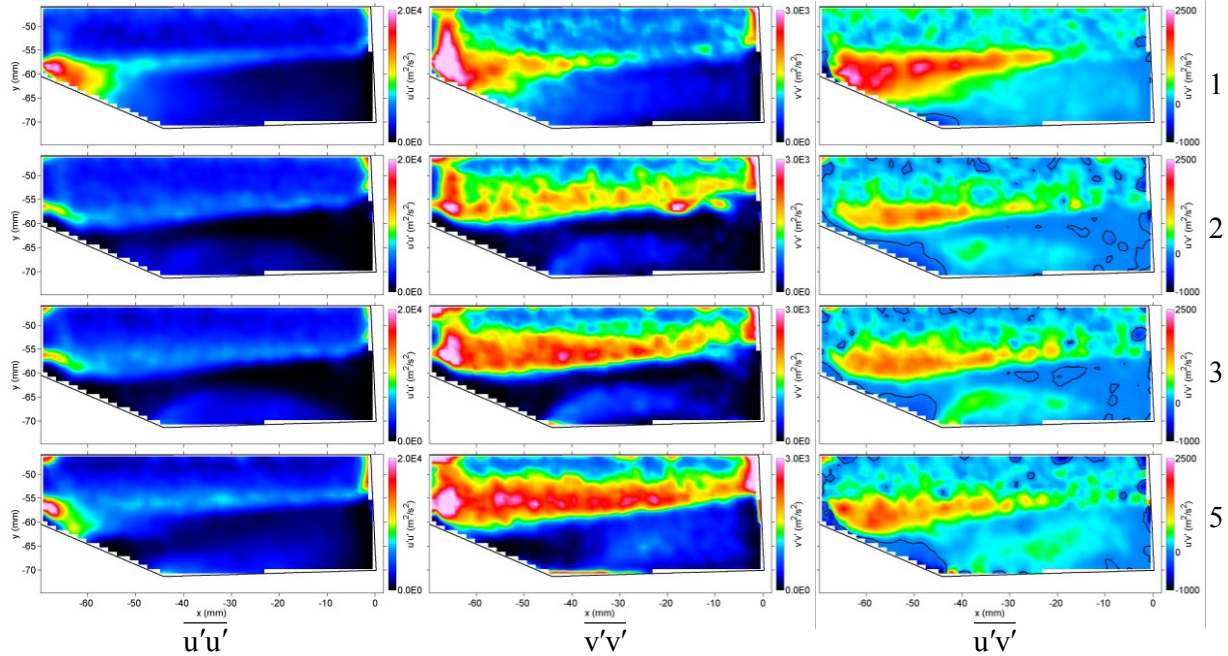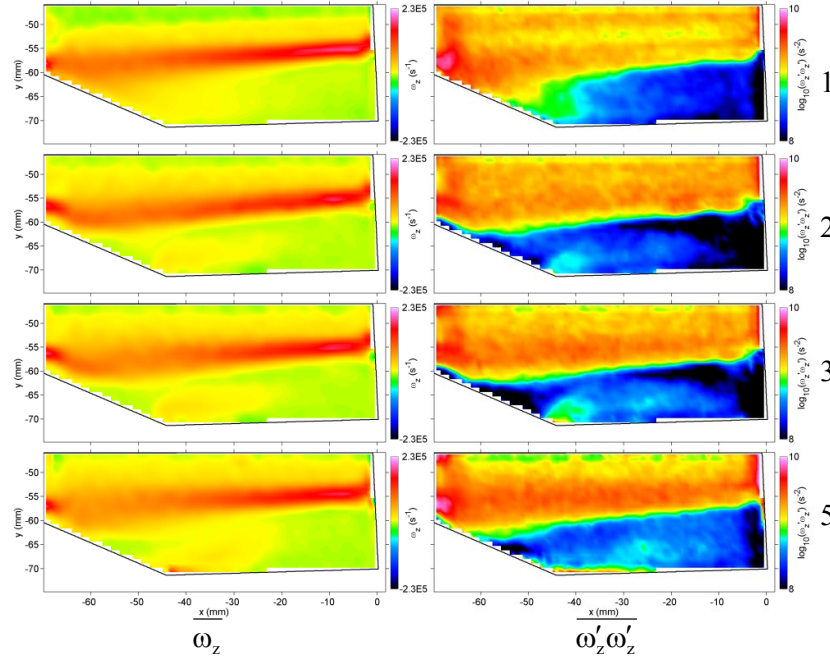

Figure 12. What is clear is that as combustion shifted downstream along the shear layer, the shear layer and cavity unsteadiness increased.

The nature of the shear layer impingement, and the associated stability, is influenced both by the shear layer combustion and combustion around the stagnation zone, both of which will attenuate vortical instability. The time-averaged results suggest a steady, stationary, persistent eddy structure at the shear layer-ramp impingement zone. The instantaneous views in Figure 6 and Figure 8, instead, suggest the formation of a convective local instability, or an unsteady bifurcation in fluid structure that is dissipated as it is convected over time and distance. Time-resolved measurements would go far to reveal how the impingement instability and the Kelvin-Helmholtz instability at the shear layer are dynamically coupled.

If we examine the averaged and variance of the vorticity for each case, shown in Figure 13, we can see how combustion changed both the shear layer and the shear layer impingement behavior. The left column shows the mean vorticity while the right shows the $\log_{10}$ of the vorticity variance. From the first column we can see that at *medium* fuel flow, Case 2, combustion has attenuated the vorticity at the separation region while creating a narrower region of higher vorticity above the ramp. Simultaneously, the corresponding vorticity variance plot shows an order magnitude decrease with combustion where the shear layer impinges the ramp and separates at the step. Furthermore, region of highest vorticity has shifted downward into the cavity, analogous to the shift of the $\bar{U}=0$ contour shown in Figure 11. The bulk flow vorticity behavior changed very little, as we would expect.

American Institute of Aeronautics and Astronautics
Approved for public release; distribution unlimited

Figure 13: Averaged and variance of the vorticity.

As the fuel flow increased and shear layer combustion shifted downstream and weakened within the cavity recirculation zone, we see can a weaker and broader region of vorticity in the mean plots and greater unsteadiness in the variance. The broader, weaker region of vorticity may be understood by the greater heat release above the ramp, which would have attenuated and broadened the local velocity gradients. The greater unsteadiness in the variance plots suggests that as the shear layer combustion shifted downstream from the separation region, it was not a steady process but that the flame shifted up and downstream along the shear layer from intermittent stability; effectively forming a lifted non-premixed flame. Such a flame is sensitive to perturbations in velocity and fuel mixture that lead to combustion instability.

IV. Conclusions

Particle image velocimetry measurements were carried out in a cavity adjacent to a supersonic, Mach-2 flow. PIV seed was injected by an angled, low momentum slot jet upstream of the cavity. Static pressure measurements along the cavity floor, with and without seed injection and combustion demonstrate that the low-momentum seed injector had minimal influence on the flow. Placing the seed in the low-momentum flow of the isolator boundary layer ensured that they would be present in the shear layer between the cavity and the bulk flow. The particles were subsequently entrained into the cavity, allowing measurements of the shear layer and cavity simultaneously, with and without combustion. The combination of the small diameter, spherical shape, and small dielectric of the TiO_2 PIV seed contributed to shear layer entrainment, quasi-uniform distribution, and minimal agglomeration. Furthermore, seeding density was sufficient to obtain velocities over the extent of the 86-mm-long cavity.

425 images were gathered in each set at *isothermal*, *medium*, *medium-high*, and *high-power* conditions, allowing a comparative study of the instantaneous and averaged, combustion-influenced velocity field. Instantaneous images revealed a highly unsteady, three-dimensional flow field for all conditions, with significant out-of-plane motion. The shear layer impingement stagnation zone at the downstream ramp produced coherent eddy structures of varying diameters; some as large as the cavity depth while others were much smaller. The eddy structures would have been convected upstream toward the shear layer separation at the upstream step. They did not appear to have a regularly spaced distribution, indicative of the acoustically coupled structures observed in other investigations and geometries. The intensity and size of these structures appeared to decrease with combustion; behavior that may be attributed to the increased viscosity, dilatation, and baroclinicity across the shear layer from combustion. The irregularity of the shear layer impingement behavior suggest either a global or convective instability, interacting and influencing the convective Kelvin-Helmholtz instability at the upstream shear layer separation through the transport of coherent structures upstream along the cavity length.

American Institute of Aeronautics and Astronautics

The average and variance of the velocity and vorticity revealed a number of behaviors that were altered by combustion and showed a dependence on the location and intensity of combustion. As would be expected in such flows, the cross-stream gradient of the streamwise velocity decreased with increasing fuel flow rates and shear layer combustion. While not apparent in the instantaneous views, the average velocity path lines revealed the primary recirculation zone predicted in time-averaged numerical investigations. The interaction of the high momentum bulk flow and the volumetric expansion accompanying heat release along the shear layer and around the ramp, where the shear layer impinged, compressed the primary recirculation zone and produced a shallower impingement angle with increasing fuel flow. The average views of the reacting cases also revealed increased out-of-plane motion at the shear layer and impingement zone with increased fuel flow rate, suggesting the presence of steady, secondary flow that could not be captured in the center plane alone.

The combination of the shallower impingement angle and the combustion-driven dilatation, baroclinicity, and dissipation changed the shear layer impingement behavior. The broadening of the shear layer with combustion and the local heat release at the ramp lengthened the ramp stagnation zone. Heat release also attenuated the unsteadiness of both the velocity and the vorticity along the shear layer, within the cavity, and where the shear layer impinged against the ramp. As the fuel flow increased and combustion stabilized further down along the shear layer, the unsteadiness of the shear layer and stagnation zone increased, suggesting that the shear layer flame was intermittently stable.

Acknowledgments

References

[1] Rasmussen, C.C., Dhanuka, S.K., Driscoll, J.F., Visualization of flameholding mechanisms in a supersonic combustor using PLIF, *Proceedings of the Combustion Institute*, (2007) 31:2505-2512.

[2] Gruber, M.R., Donbar, J.M., Carter, C.D., Hsu, K.-Y., Mixing and Combustion Studies Using Cavity-Based Flameholders in a Supersonic Flow, *Journal of Propulsion and Power*, (2004) 20:5:769-778.

[3] Micka, D.J., Driscoll, J.F., Combustion characteristics of a dual-mode scramjet combustor with cavity flameholder, *Proceedings of the Combustion Institute*, (2009) 32:2397-2404.

[4] Hsu, K.-Y., Carter, C.D., Gruber, M.R., Barhorst, T., Smith, S., Experimental Study of Cavity Strut Combustion in Supersonic Flow, *Journal of Propulsion and Power*, (2010) 26:6:1237-1246.

[5] Scheel, F., PIV Measurement of a 3-Dimensional Reacting Flow in a Scramjet Combustion Chamber, 42nd AIAA Aerospace Sciences Meeting and Exhibit, (2004) AIAA-2004-1038.

[6] Lahr, M.D., Pitz, R.W., Douglas, Z.W., Carter, C.D., Hydroxyl-Tagging-Velocimetry Measurements of a Supersonic Flow over a Cavity, *Journal of Propulsion and Power*, (2010) 26:4:790-797.

[7] Coats, C.M., Coherent Structures in Combustion, *Progress in Energy and Combustion Science*, (1996) 22:5:427–509.

[8] Mehta, P.G., Soteriou, M.C., Combustion Heat Release Effects on yhe Dynamics Of Bluff Body Stabilized Premixed Reacting Flows, 41st AIAA Aerospace Sciences Meeting and Exhibit, (2003) AIAA-2003-0835.

[9] Erickson, R.R., Soteriou, M.C., Mehta, P.G., The Influence of Temperature Ratio on the Dynamics of Bluff Body Stabilized Flames, 44th AIAA Aerospace Sciences Meeting and Exhibit, (2006) AIAA-2006-753.

[10] Ünalmis, Ö.H., Clemens, N.T., Dolling, D.S., Planar Laser Imaging of a Supersonic Side-Facing Cavity, 37th AIAA Aerospace Sciences Meeting and Exhibit, (1999) AIAA-1999-0297.

[11] Gruber, M. R., Nejad, A. S., New Supersonic Combustion Research Facility, *Journal of Propulsion and Power*, (1995) 11:5:1080–1083.

[12] Lin, K.-C., Tam, C.-J., Boxx, I., Carter, C.D., Jackson, K., Lindsey, M., Flame Characteristics and Fuel Entrainment Inside a Cavity Flame Holder in a Scramjet Combustor, 43rd AIAA/ASME/SAE/ASEE Joint Propulsion Conference and Exhibit, 2007, AIAA-2007-5381.

[13] Fuchs, N. A., *The Mechanics of Aerosols*, Dover Publications, New York (1989).

[14] Urban, W.D., Mungal, M.G., 35th AIAA Aerospace Sciences Meeting and Exhibit, (1997) AIAA-1997-0757.

[15] Erbland, P.J., Development and Application of Carbon Dioxide Enhanced Raylegh Scattering for High Speed Low Density Flows, Ph.D. Thesis, Princeton University, Princeton, NJ, 2000.

[16] ASM Engineered Materials Reference Book, Second Edition, Michael Bauccio, Ed. ASM International, Materials Park, OH, 1994.

American Institute of Aeronautics and Astronautics

[17] Oxides and Hydroxides of Aluminum, Alcoa Technical Paper No. 19, Revised, Karl Wefers and Chanakya Misra, Alcoa Laboratories, 1987.

[18] CRC Handbook of Chemistry and Physics, David R. Lide, Ed. 80th Edition, CRC Press, Boca Raton, FL, 1999.

[19] Raffel, M., Willert, C., Wereley, S., Kompenhans, J., *Particle Image Velocimetry A Practical Guide*, 2nd Ed., Springer-Verlag, Berlin-Heidelberg (2007).

[20] Product Manual, FlowMaster DaVis 7.2, Göttingen (2007).

[21] Kundu, P.K., *Fluid Mechanics*, Academic Press (1990) San Diego, CA, USA.

[22] Rossiter, J.E., Wind-Tunnel Experiments on the Flow Over Rectangular Cavities at Subsonic and Transonic Speeds, Aeronautical Research Council, Repts. and Memoranda No. 3438, London, Oct. 1964.

[23] Rowley, C.W., Williams, D.R., Dynamics and Control of High-Reynolds-Number Flow over Open Cavities, *Annual Reviews of Fluid Mechanics*, (2006) 38:251-276.

[24] Gruber, M.R., Baurle, R.A., Mathur, T., Hsu, K.-Y., Fundamental Studies of Cavity-Based Flameholder Concepts for Supersonic Combustors, *Journal of Propulsion and Power*, (2001) 17:1:146-153.

[25] Meliga, P., Chomaz, J.-M., Global modes in a confined impinging jet: application to heat transfer and control, *Theoretical and Computational Fluid Mechanics* (2011) 25:179-193.

[26] Huerre, P., Monkewitz, P.A., Local and global instabilities in spatially developing flows, *Annual Reviews of Fluid Mechanics* (1990) 22:473-537.

[27] Prasad, A., Williamson, C.H.K., The instability of the shear layer separating from a bluff body, *Journal of Fluid Mechanics* (1997) 333:375-402.

[28] Mehta, P.G., Soteriou, M.C., Combustion Heat Release Effects on the Dynamics of Bluff Body Stabilized Premixed Reacting Flows, 41st AIAA Aerospace Sciences Meeting and Exhibit (2003) AIAA-2003-0835.

[29] Freeborn, A.B., King, P.I., Gruber, M.R., Swept-Leading-Edge Pylon Effects on a Scramjet Pylon-Cavity Flameholder Flowfield, *Journal of Propulsion and Power*, 25:3:571-582.

[30] Harrington, J.E., Smyth, K.C., Laser-Induced Fluorescence Measurements of Formaldehyde in a Methane/Air Diffusion Flame, *Chemical Physics Letter*, (1993) 202:3,4:196-202.